Electronic Supplementary Material (ESI) for ChemComm.


Electronic Supplementary Information

# Interlocked multi-armed carbon for stable oxygen reduction

Yiming Li,[a] Lei Li,[a] Longfeng Zhu,[a] Li Gu*[b] and Xuebo Cao*[a]

[a] *School of Biology and Chemical Engineering, Jiaxing University, Jiaxing, Zhejiang 314001, China. E-mail: xbcao@mail.zjxu.edu.cn.*

[b] *School of Materials and Textile Engineering, Jiaxing University, Jiaxing, Zhejiang, 314001, China. E-mail: guli@mail.zjxu.edu.cn.*

## Experimental Section

**Materials:** Zinc nitrate hexahydrate ($Zn(NO_3)_2 \cdot 6H_2O$, 99.0%, Aladdin Reagent), 2-methylimidazole ($C_4H_6N_2$, 98.0%, Aladdin Reagent), methanol ($CH_3OH$, ≥99.5%, Sinopharm Chemical Reagent Co. Ltd), N,N-dimethylformamide, ($C_3H_7NO$, ≥99.5%, Sinopharm Chemical Reagent Co. Ltd) and nafion solution(5%, DuPont) were used as purchased, without any further purification.

**Preparation of multi-armed ZnO (MAZ):** MAZ was synthesized according to our previous report.[S1] In a typical experiment, 2.97 g $Zn(NO_3)_2 \cdot 6H_2O$ and 4.48 g KOH were dissolved with 20 mL deionized water respectively. Then, the aqueous solution of zinc salt was added into KOH solution under stirring to give a transparent solution and was placed in an over with the temperature set at 75 ºC for 10 h. The MAZ was separated from the solution, washed with deionized water and dried in vacuum for further templating process.

**Preparation ZnO@ZIF-8 hybrid:** 10 mL methanol solution of 2-methylimidazole (0.1 mol $L^{-1}$) and 0.1 g MAZ were added into a 50 mL Teflon-lined stainless steel autoclave, which was closed and maintained at 80 ºC for 4 h to yield ZnO@ZIF-8. After cooling down to room temperature, the ZnO@ZIF-8 was precipitated from the solution and then washed three times by ethanol and deionized water in sequence. Finally, the ZnO@ZIF-8 was obtained after freeze-drying.

**Preparation of multi-armed carbon (MAC):** The as prepared ZnO@ZIF-8 was heated to 200 ºC for 2 h at a heating rate of 3 ºC $min^{-1}$, and then performed at 550 ºC for 3 h under nitrogen gas flow to yield ZnO@C. The ZnO@C powder was immersed in HCl (0.1 mol $L^{-1}$) overnight to remove the ZnO template and Zn species. The multi-armed carbon (MAC) was obtained by washing with deionized water and after freeze-drying. The further pyrolysis treatment was performed at 950 ºC for 3 h under nitrogen atmosphere at a heating rate of 2 ºC $min^{-1}$ to give MAC-950. For comparison, MAC-650, MAC-750 and MAC-850 were synthesized by the similar procedure, except the pyrolysis temperatures were changed to 650 ºC, 750 ºC and 850 ºC, respectively.

**Characterization:** Scanning electron microscopy (SEM) was performed on a Hitachi S-4800 instrument, operating at the accelerating voltage of 20 kV. Transmission electron microscope (TEM) and high-resolution transmission electron microscopy (HRTEM) characterization were performed on an FEI Tecnai G20 electron microscope operating at 200 kV. Powder X-ray diffraction (XRD) data were recorded from a Bruker D8 Focus Powder X-ray diffractometer using Cu Kα radiation

(40 kV, 40 mA). $N_2$ sorption analysis was conducted using TriStar 3020 and Micrometritics ASAP 2020 at 77 K, and the surface area was calculated by using Barrett-Emmett-Teller (BET). X-ray photoelectron spectra (XPS) were obtained with an ESCALab220i-XL electron spectrometer from VG Scientific using 300W Al Kα radiation. Raman scattering spectra were acquired using a LabRAM HR800 Raman spectrometer with a 632.8 nm wavelength incident laser. Conductivity measurements of the 3DPCs were measured by a two-probe method.

**Electrochemical measurements:** All the electrochemical characterizations were performed in 0.1 M KOH solution using a three-electrode system on an AUT128N electrochemical workstation (Metrohm, Switzerland). A platinum foil and Ag/AgCl (3.5 M KCl) used as counter and reference electrodes, respectively. A glassy carbon disk of 5.0 mm in diameter served as the substrate for the working electrodes. The catalysts (2 mg) were dispersed in N, N-Dimethylformamide (1.0 mL) with adding Nafion solution (5 wt%, 0.05 mL), to form a well-dispersed ink. A certain volume of catalyst ink was drop-casted onto the surface of electrode with loading 0.1 mg $cm^{-2}$ for all samples and dried at 50 ºC. The cyclic voltammetry (CV) tests were cycled between -0.8 and 0.3 V at room temperature in $N_2$-and $O_2$- saturated 0.1 M KOH solution with a scan rate of 50 mV $s^{-1}$. Rotating disk electrode (RDE) experiments were carried out in $O_2$- saturated 0.1 M KOH solution at room temperature, a sweep rate of 10 mV $s^{-1}$ and different speed rates (400-2400 rpm). For comparison, commercial Pt/C (20 wt%, Johnson Matthey) was conducted on same electrochemical tests. The measured potentials vs. Ag/AgCl were converted to a reversible hydrogen electrode (RHE) scale according to the Nernst equation ($E_{RHE} = E_{Ag/AgCl} + pH \times 0.059 + 0.1976$ V).

The electron transfer number can be calculated by the Koutecky-Levich equation [S2]:

$$\frac{1}{j} = \frac{1}{j_k} + \frac{1}{B\omega^{1/2}} \quad (1)$$

$$B = 0.62nFC_0(D_0)^{2/3}\nu^{-1/6} \quad (2)$$

$$j_k = nFkC_0 \quad (3)$$

Where $j$ is the measured current density, $j_k$ is the kinetic current density, $\omega$ ($\omega = 2\pi N$, N is the rotation speed) is the electrode rotating rate, $F$ is the Faraday constant (96485 C $mol^{-1}$), $C_0$ is the bulk concentration of $O_2$ ($1.2 \times 10^{-6}$ mol $cm^{-3}$), $D_0$ is the diffusion coefficient of $O_2$ ($1.9 \times 10^{-5}$ $cm^{-2}$

$s^{-1}$), and $v$ is the kinematic viscosity of the electrolyte (0.01 $cm^{-2}$ $s^{-1}$), $k$ is the electro transfer rate constant, and $n$ represents the overall number of electrons transferred in oxygen reduction.[S3]

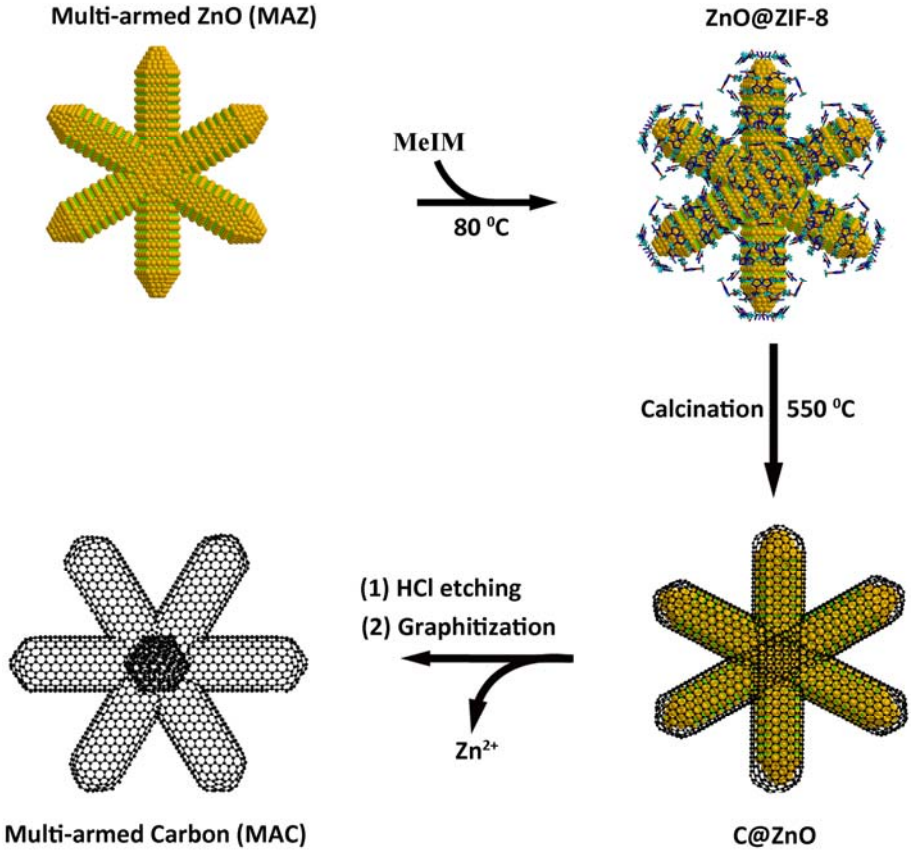


**Scheme S1.** Illustration of the preparation of multi-armed carbon (MAC). With multi-armed ZnO as solid zinc source and sacrificial scaffold, ZIF-8 could deterministically grow on the active surface of ZnO. The resultant ZnO@ZIF-8 hybrid could be derived into MAC via a two-step pyrolysis process.

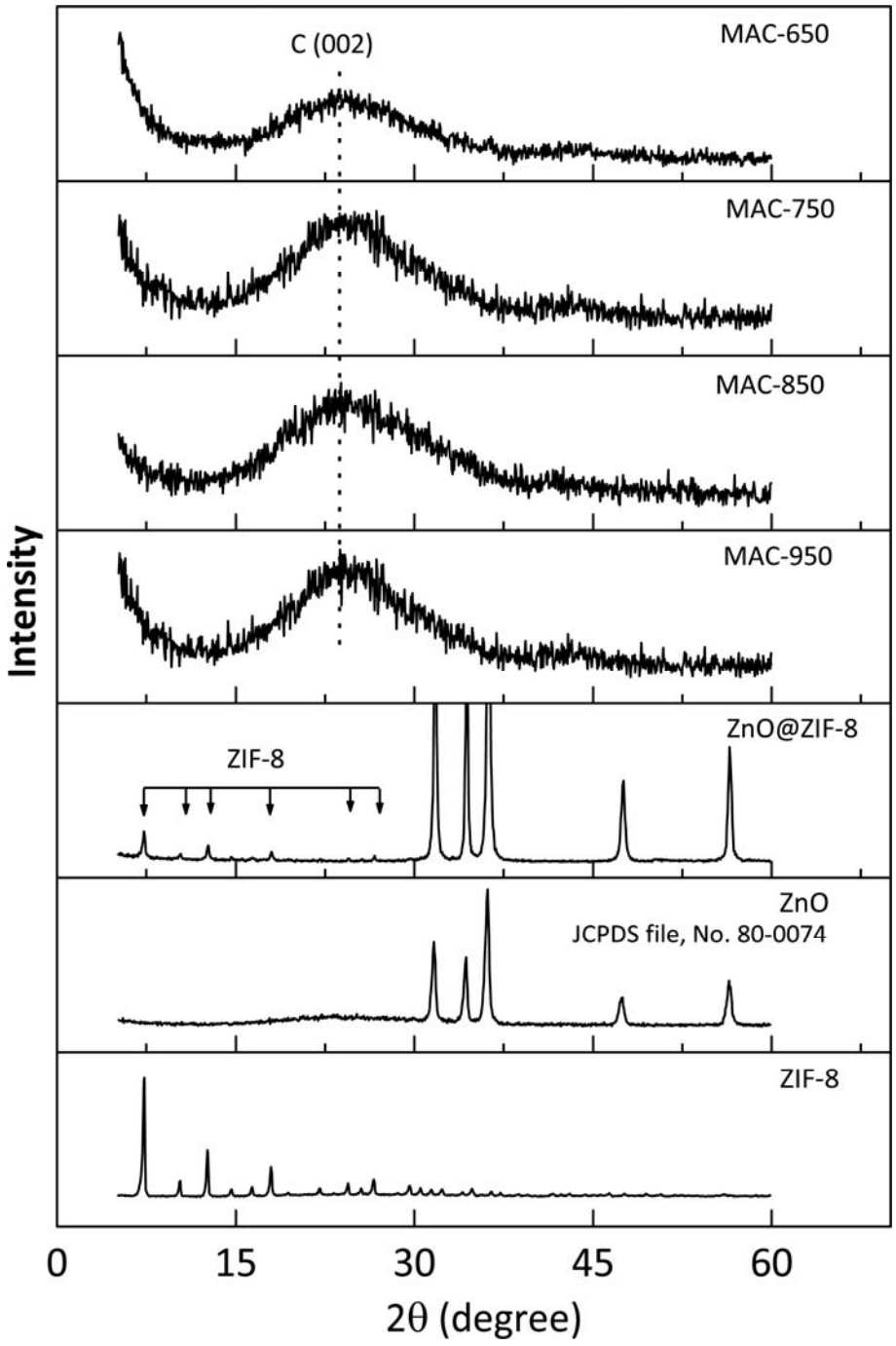


**Fig. S1** XRD patterns for multi-armed ZnO (referred to as MAZ), ZnO@ZIF-8, and multi-armed carbon graphitized at 650 ºC, 750 ºC, 850 ºC, and 950 ºC (referred to as MAC-650, MAC-750, MAC-850, and MAC-950, respectively). The standard XRD pattern of ZIF-8 was included for reference.

As seen, only the peak at around 25.8º representing the interplane (002) reflection of graphite carbon is observed. The result demonstrates that ZIF-8 was successfully converted into carbon and there are no impurities of the species such as Zn and ZnO.

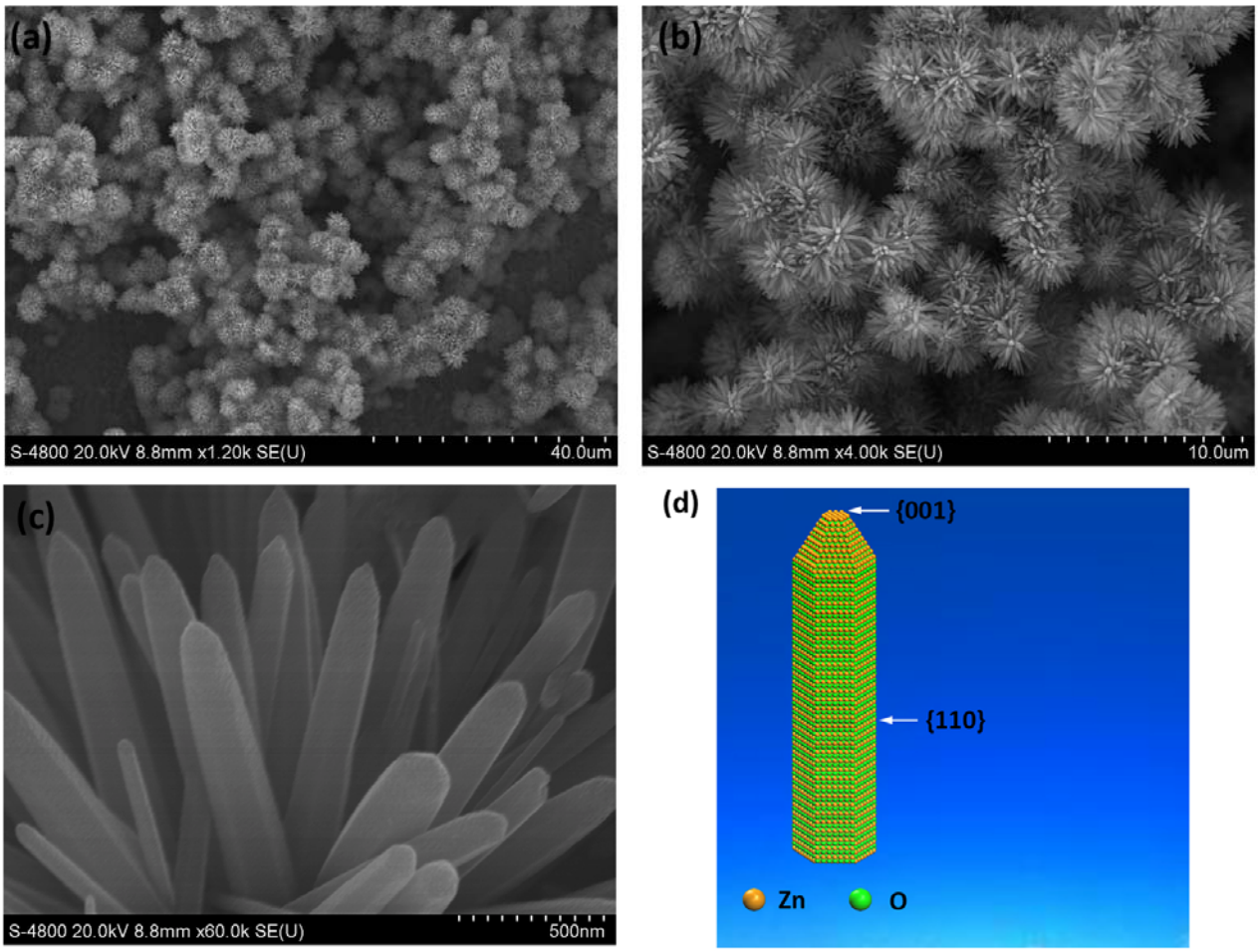


**Fig. S2** (a, b) SEM images at low and high magnification show the multi-armed morphology and uniformity of MAZ. (c) A close look of the arms for MAZ. (d) Schematic diagram of the arm of MAZ. The exposed Zn atoms make the surface of MAZ be active, thus able to induce the deterministic nucleation and growth of ZIF-8.

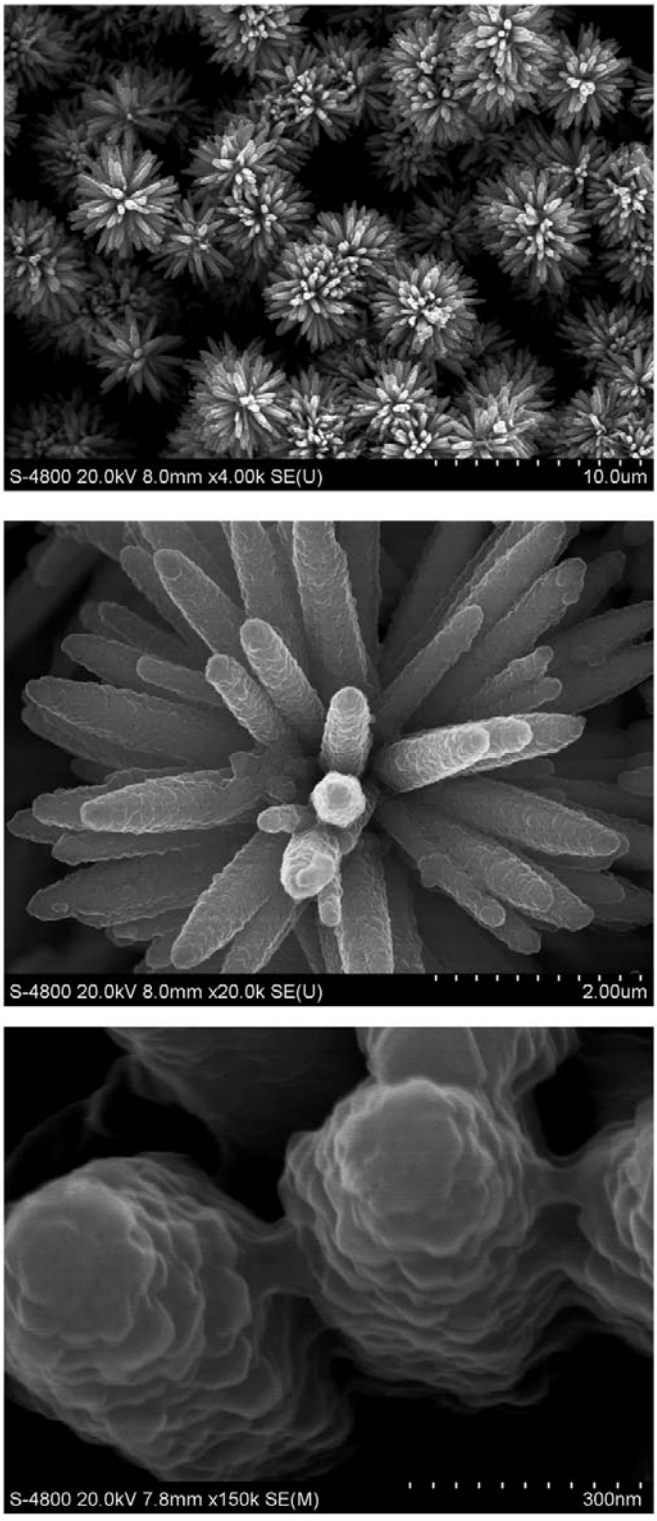


**Fig. S3** SEM images of ZnO@ZIF-8. Owing to the deterministic growth of ZIF-8 on the active surface of MAZ, the morphology of MAZ was well replicated by ZnO@ZIF-8. However, the surfaces of the arms were no longer smooth because of the coating of ZIF-8.

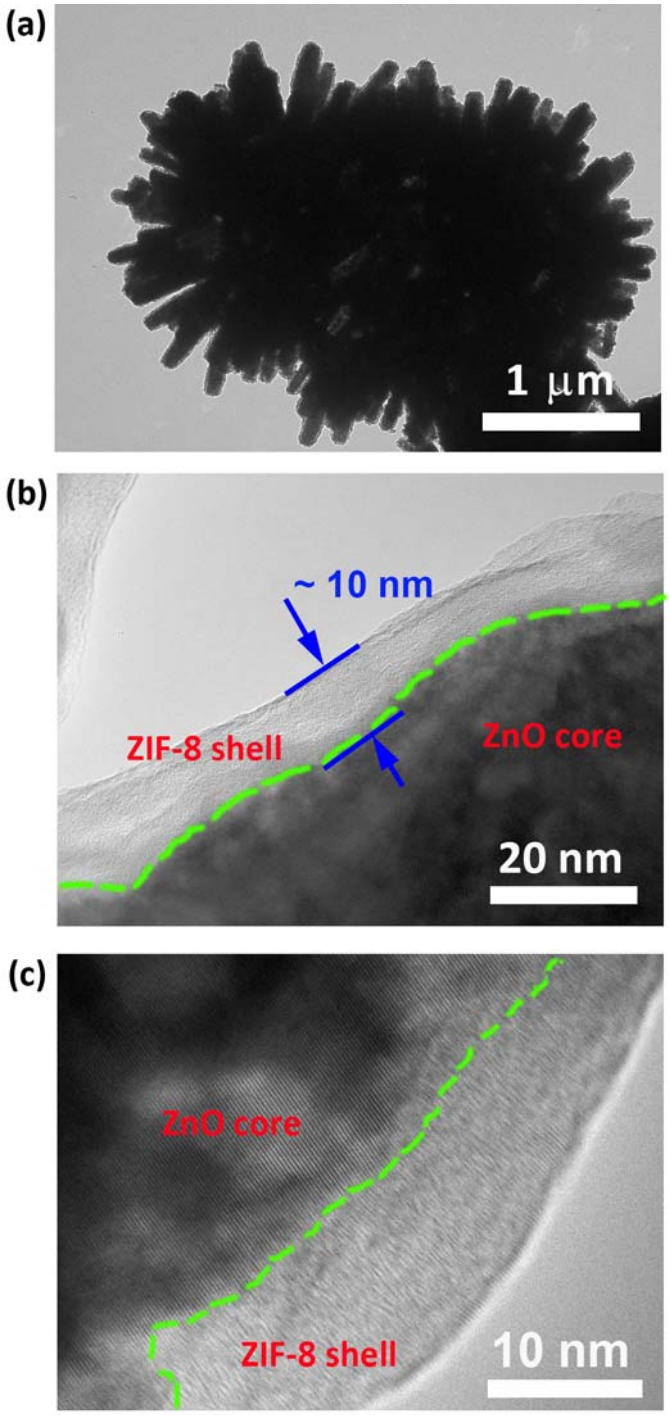


**Fig. S4** (a) TEM image of ZnO@ZIF-8. (b and c) High-magnification TEM images of ZnO@ZIF-8. It is clearly seen that ZnO@ZIF-8 is the hybrid composed of crystalline ZnO core and ZIF-8 shell with thickness around 10 nm.

It should be noted that our strategy is very efficient in the growth of very thin ZIF-8 because of the following factor. Once MAZ is covered by a layer of ZIF-8, the diffusion of Zn atoms from the core to the surface will be greatly retarded, thus passivating the surface of MAZ and restricting the continuous growth of ZIF-8.

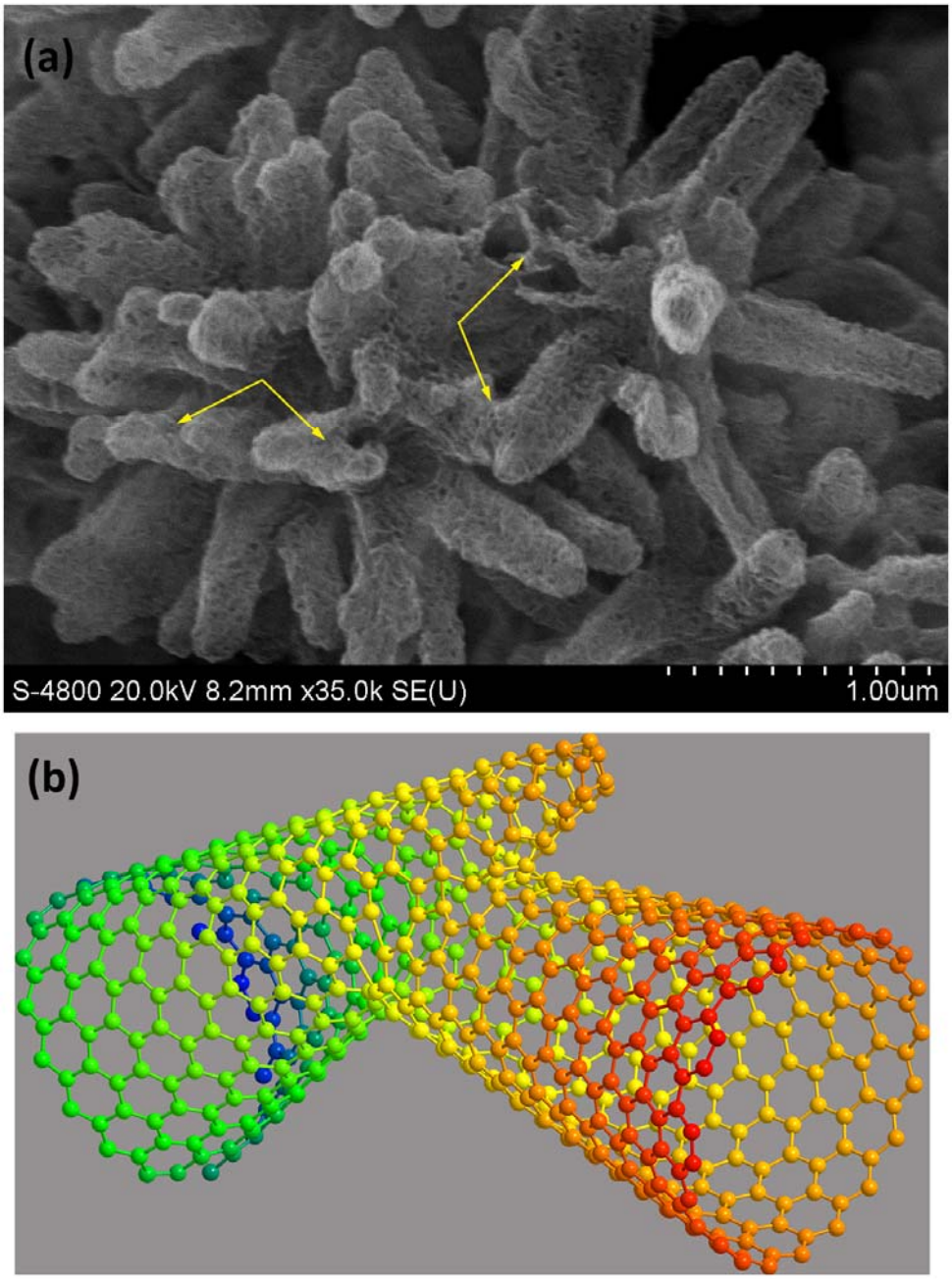


**Fig. S5** (a) SEM image shows the arm-arm junctions (indicated by the arrows) and the abundant mesopores and macropores in MAC. (b) Schematic diagram of the arm-arm junction.

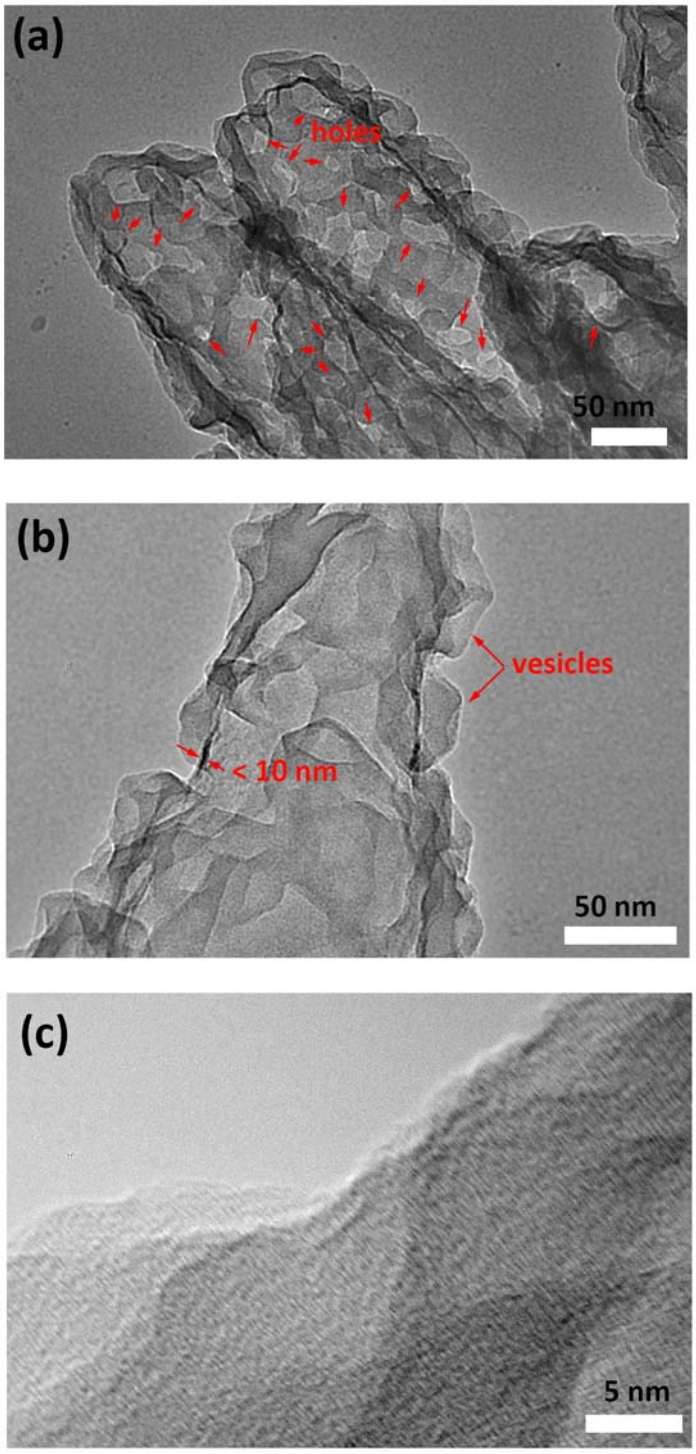


**Fig. S6** (a) TEM image show the presence of abundant holes on the arm of MAC. (b) TEM image shows the vesicles attached on the wall of the arm of MAC. (c) HRTEM image shows the thin wall for the arm of MAC.

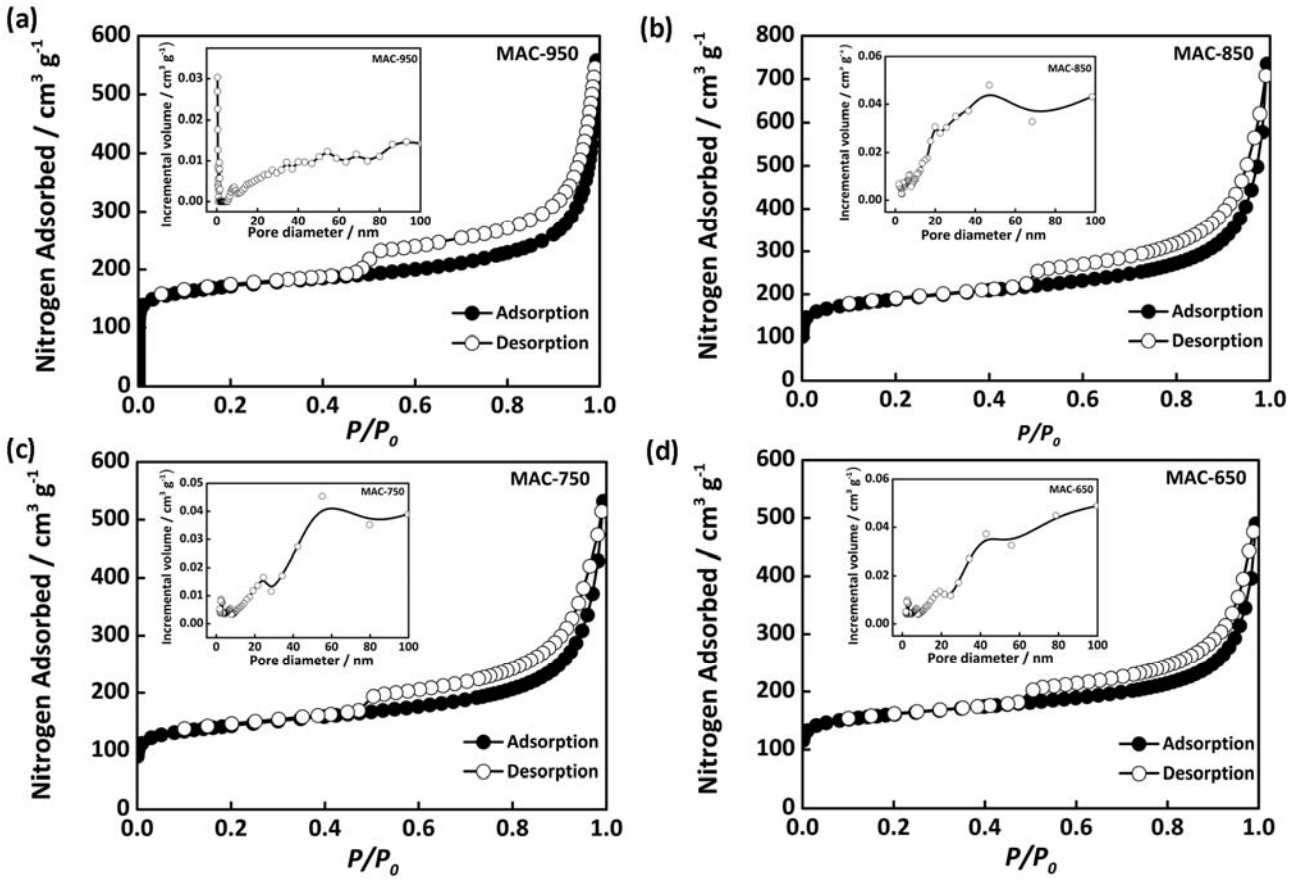


**Fig. S7** $N_2$ adsorption-desorption isotherms of MAC-950 (a), MAC-850 (b), MAC-750 (c), and MAC-650 (d). Insets show the corresponding pore distribution curves.

As seen, all the samples exhibit the type-IV isotherms with a pronounced hysteresis loop in the $P/P_0$ range of 0.5 ~ 1.0, indicating the formation of mesoporous structure. From the pore-distribution curves, all the MACs have a broad pore distribution ranging from several nanometers to several tens of nanometers and their characteristics are analogous. The mesopores below 10 nm might originate from porous ZIF-8 and the evaporation of Zn in ZIF-8[S4]. The pores above 10 nm might originate from the gaps between the neighboring arms as well as the hollow structure of the arms after ZnO removal.

**Table S1** Brunauer−Emmett−Teller (BET) surface area and total pore volume for the four MACs[a]

| Sample | MAC-650 | MAC-750 | MAC-850 | MAC-950 |
|---|---|---|---|---|
| BET ($m^2 g^{-1}$) | 548 | 493 | 647 | 590 |
| Pore Volume ($cm^3 g^{-1}$) | 0.60 | 0.67 | 0.83 | 0.62 |

[a] Generally, the BET surface area of nanoporous carbon derived from ZIF-8 exceeds 1000 $m^2/g$. Herein, the much smaller BET surface area of the four MACs is correlated to the very thin arm of the MACs. Since the arms of MACs are very thin, the pore walls are easily damaged by the high temperature, leading to the conversion of micropores to mesopores and macropores. As a result, the BET specific surface areas of MACs are dramatically decreased.

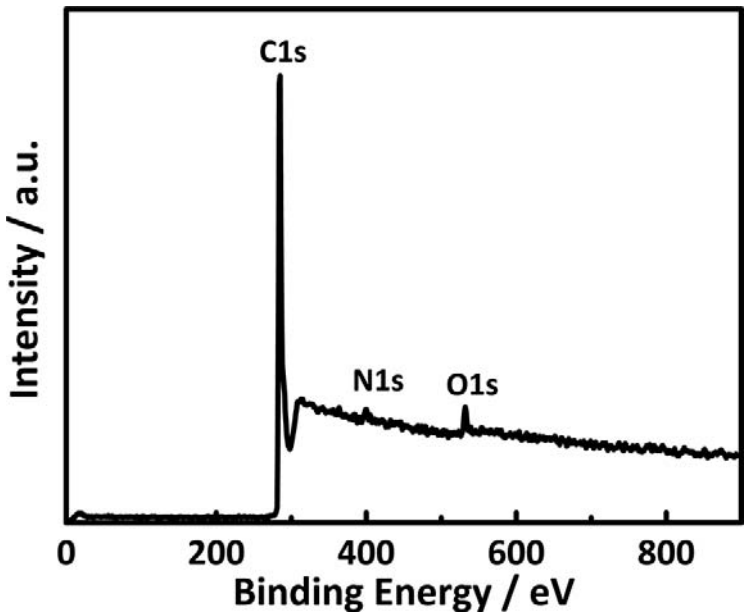


**Fig. S8** XPS survey spectrum for MAC-950. Only the elements of C, O, and N were detected. The survey spectra for MAC-850, MAC-750, and MAC-650 are similar and not sown.

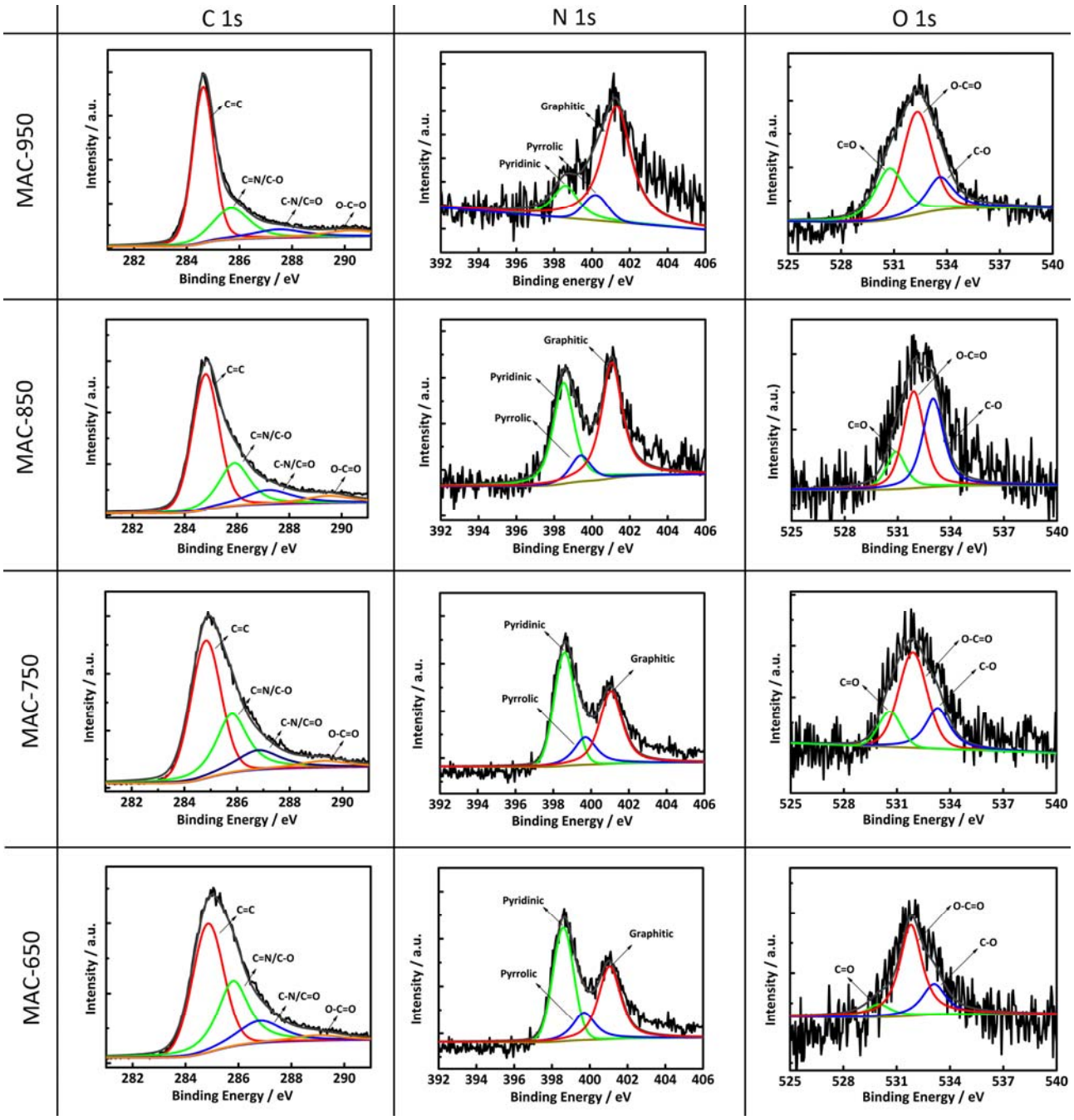


**Fig S9** High-resolution C1s, N 1s, and O 1s spectra for MAC-950, MAC-850, MAC-750, and MAC-650

The C 1s spectra clearly demonstrate that the increase of the pyrolysis temperature can increase the graphitization degree of MACs, consistent with the results of conductivity measurements. The N 1s spectra reveal that, with the increase of the pyrolysis temperature, the portion of graphitic-*N* is increased while the pyridinic-*N* is decreased. This is because the pyridinic groups are not thermally stable and they convert to pyrrolic-*N* and graphitic-*N* at higher annealing temperatures [S5]. As for the O 1s spectra of the MACs, there is no notable difference.

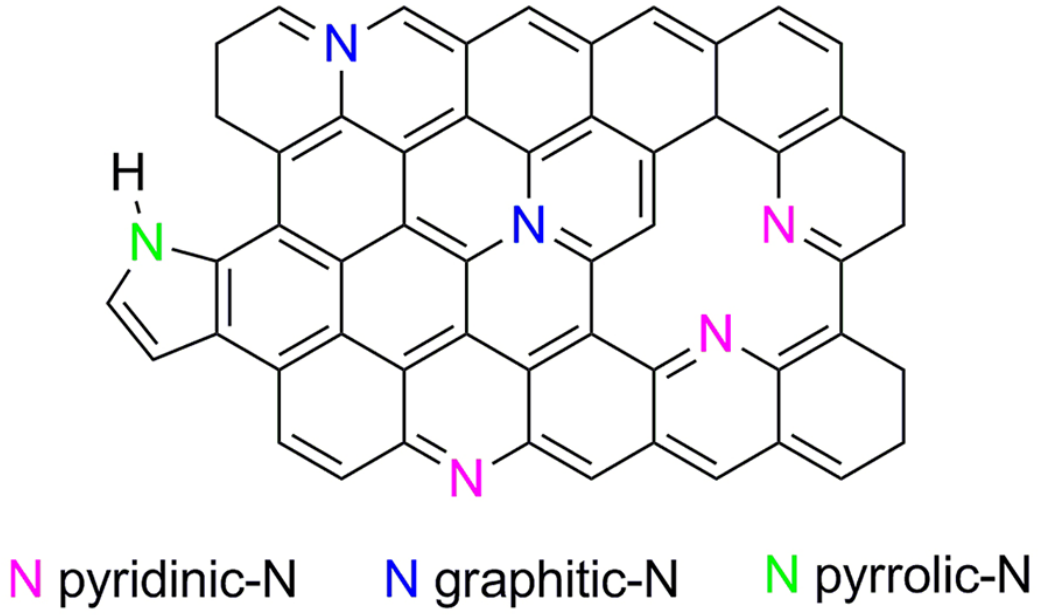


**Fig. S10** Representation of different *N*-based functional groups

**Table S2** C, O, and N contents in MACs [a]

| Sample | Oxygen Content (at. %) | Carbon Content Total (at.%) | | Nitrogen Content Total (at.%) | | |
|---|---|---|---|---|---|---|
| | | $sp^2$ C | Other C species | Pyri-N | Pyrro-N | Grap-N |
| MAC-650 | 4.1 | 74.5 | | | 21.4 | |
| | | 36.06 | 38.44 | 12.43 | 1.67 | 7.30 |
| MAC-750 | 4.5 | 80.1 | | | 15.7 | |
| | | 40.77 | 39.33 | 7.37 | 1.80 | 6.53 |
| MAC-850 | 4.2 | 86.0 | | | 9.8 | |
| | | 47.56 | 38.44 | 3.94 | 1.01 | 4.85 |
| MAC-950 | 5.4 | 89.9 | | | 4.7 | |
| | | 52.82 | 37.08 | 0.82 | 0.46 | 3.42 |

[a] Quantitative analysis of C, N and O species were based on the deconvolution results of the high-resolution C 1s, O 1s, and N 1s spectra [S6]. The results reveal that the O content is almost constant, while C and N contents are changed oppositely, which are consistent with previous observations [S7]. The serious nitrogen loss is due to the instability of nitrogen at high temperature.

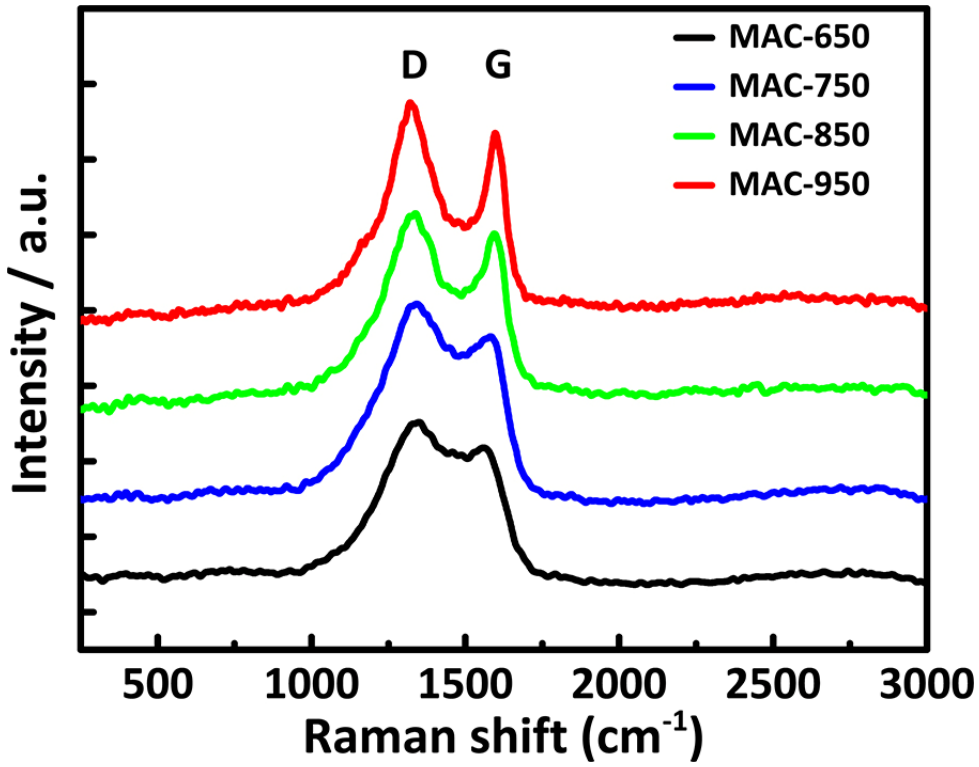


**Fig. S11** Raman spectra for MAC-650, MAC-750, MAC-850, and MAC-950.

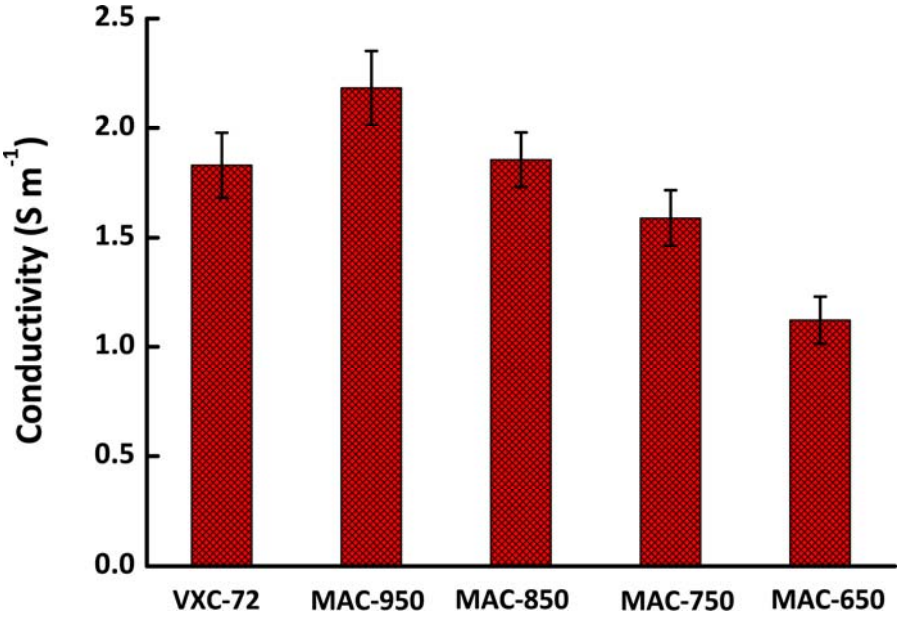


**Fig. S12** Conductivity comparison among our MAC and VXC-72 which is the most widely used support of Pt catalysts. The bar plots are averages of three replicates and the error bars are the standard derivations.

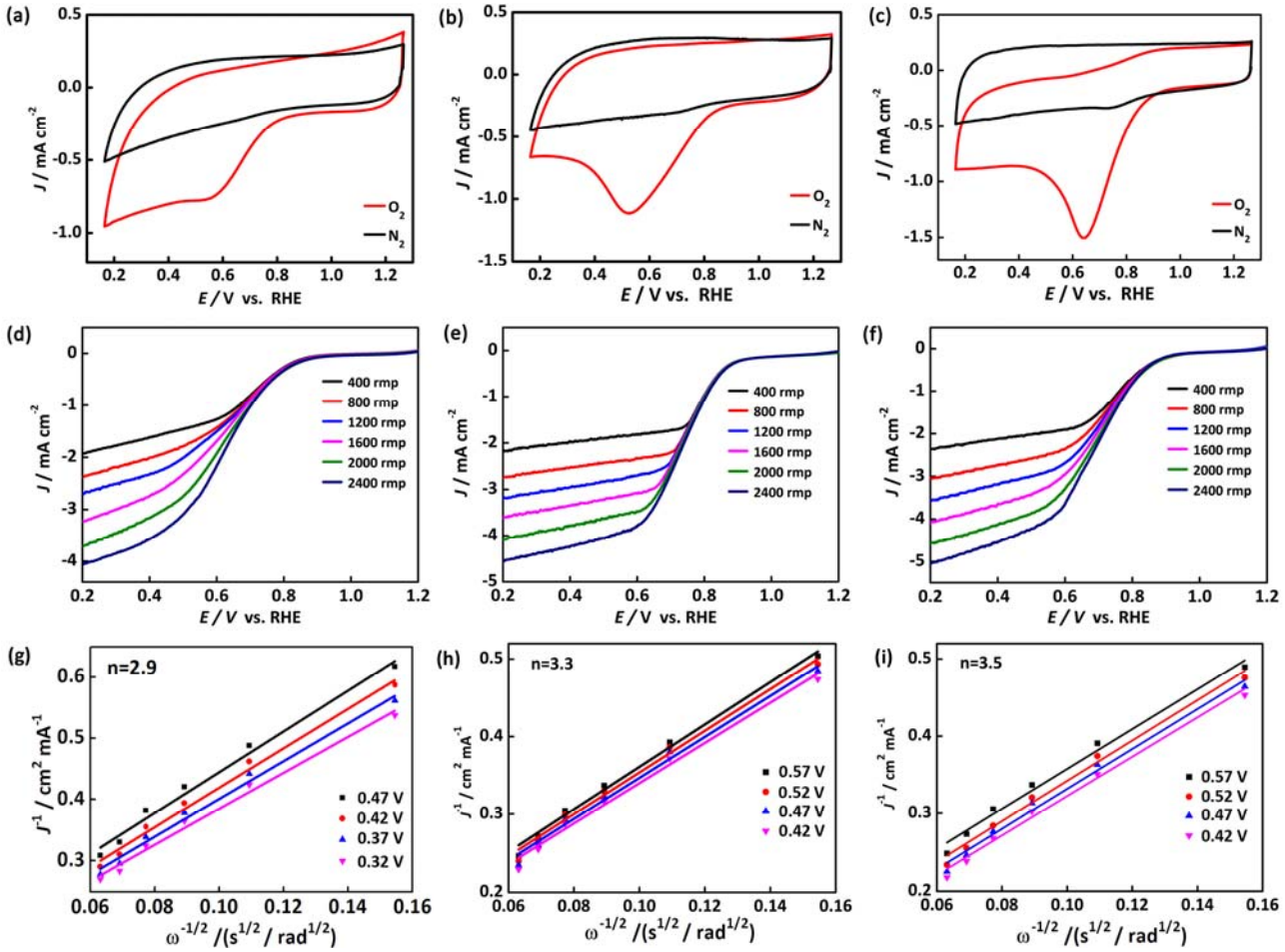


**Fig. S13** (a-c) CV curves of MAC-650, MAC-750, and MAC-850. (d-f) *LSV* curves of MAC-650, MAC-750, and MAC-850. (g-i) Kouteck-Levich plots of MAC-650, MAC-750, and MAC-850 derived from RDE data at different electrode potentials.

Up to now, there is no consensus on the essential factors that are responsible for the ORR activity of nitrogen doped nanoporous carbon. All the factors, such as the *N* content, the ratio of graphitic-*N* and pyridinic-*N* to pyrrolic-*N*, the electron transfer ability, and the mass transfer ability, all affect the ORR activities. It is now clear that only the high *N* content cannot assure high ORR performance. The high ratio of graphitic-*N* and pyridinic-*N* to pyrrolic-*N* is more important. Herein, MAC-950 exhibits a better ORR performance among the four MACs. However, it has the lowest N content among the four samples and a close ratio of graphitic-*N* and pyridinic-*N* to pyrrolic-*N* (11.8, 7.7, 8.7, and 9.2 for MAC-650, MAC-750, MAC-850, and MAC-950, respectively). We thus believe that the better conductivity of MAC-950 plays a critical role in enhancing its ORR performance, which promotes the electron transfer to the active sites[S8].

Furthermore, there exists an abnormal phenomenon for the ORR performances of MAC-750 and MAC-850: MAC-750 has lower overpotential than MAC-850, while MAC-850 shows larger

limiting current density. This phenomenon always appears in the repeated experiments. The larger limiting current density of MAC-850 than MAC-750 should be the consequence of the relatively large BET surface (647 $m^2/g$ vs. 493 $m^2/g$), which offers more active sites for ORR at the large bias. Very recently, pyridinic-N was found to create the active sites and reduce the ORR overpotential [S9]. Consequently, the relatively small overpotential of MAC-750 to MAC-850 may be attributed to the higher pyridinic-N content (7.37% vs. 3.94%), which facilitates the occurrence of ORR. It should emphasize that the factors responsible for the ORR activity are multiple. Besides pyridinic-N and the BET surface area mentioned above, other parameters, such as the N content, graphitic-N, and the transfer abilities of mass and electron, are also critical. And only a delicate balance is realized, a maximized ORR activity can be achieved, such as MAC-950.

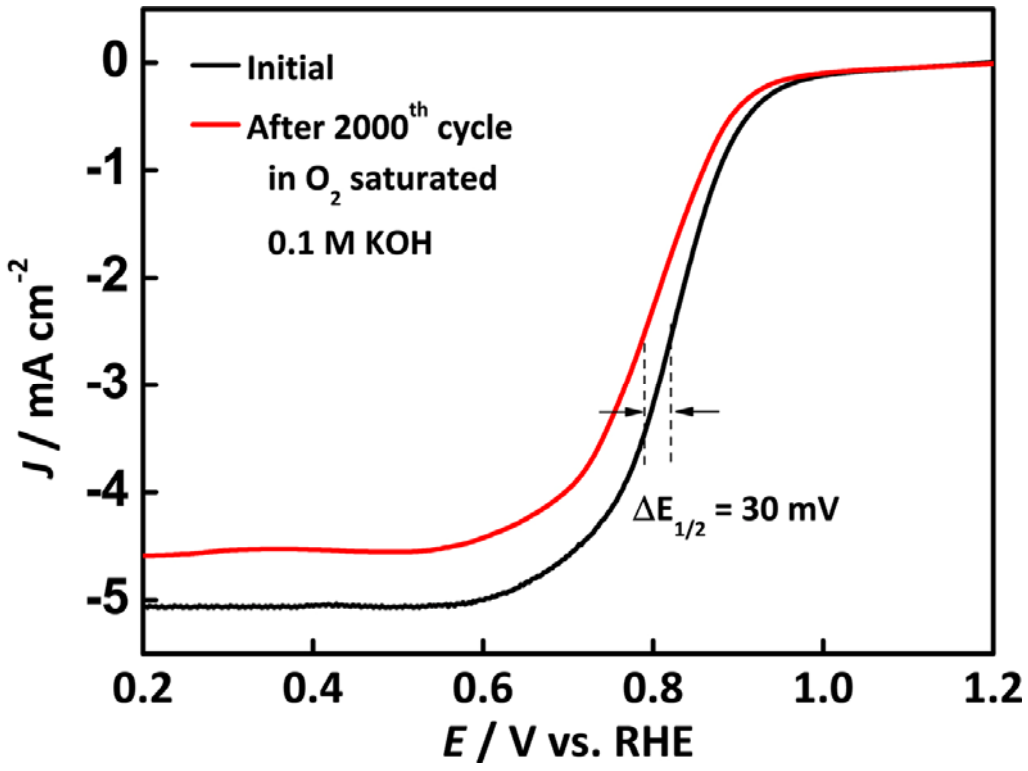


**Fig. S14.** LSV curves of Pt/C after 2000 potential cycles in $O_2$ saturated electrolyte.

**Table S3.** Comparison of ORR performance of MAC-950 with other NPC materials in literatures.

| Materials | Onset potential V *vs.* RHE (compare to Pt/C) | Half potential V *vs.* RHE (compare to Pt/C) | Electron transfer number | Reference |
|---|---|---|---|---|
| MAC-950 | 0.886 (50 mV negative) | 0.766 (50 mV negative) | 3.8 | Present Work |
| N,S-co-doped grapheme mesh | 0.04 (vs. Ag/AgCl) (10 mV negative) | (more than120 mV negative) | 3.6 | *Energy Environ. Sci*., **2014**, 7, 1913 |
| N-doped carbon nanocage | -0.13 (vs. Ag/AgCl) (100 mV negative) | - | 3.27 | *Adv. Mater*., **2012**, 24, 5593 |
| NGSH | 0.88 (80 mV negative) | - | 3.3 | *Small,* **2014**, 10, 2251 |
| N-doped 3D graphene | -0.08 (vs. Ag/AgCl) (not mentioned) | - | 3.9 | *Adv. Mater*., **2014**, 26, 4145 |
| N-doped carbon nanosheets | -0.01 (vs. Ag/AgCl) (10 mV negative) | -0.11 (vs. Ag/AgCl) (40 mV negative) | 3.8 | *Angew. Chem. Int. Ed*., **2014**, 53, 1570 |
| NGPC-1000-10 | -0.02 (vs. Ag/AgCl) (40 mV negative) | -0.20 (vs. Ag/AgCl) (40 mV negative) | 3.81 | *Nanoscale*, **2014**, 6, 6590. |
| P-Z8-Te-1000 | -0.07 (vs. Ag/AgCl) (10 mV positive) | -0.161 (vs. Ag/AgCl) (31 mV positive) | ~4.0 | *J. Am. Chem. Soc*., **2014**, 136, 14385 |
| Carbon-L | 0.861 (63 mV negative) | 0.697 (102 mV negative) | 3.68 | *Energy Environ. Sci*., **2014**, 7, 442 |
| CNF@NG | 0.93 (100 mV negative) | 0.80 (80 mV negative) | 3.6 | *Angew. Chem. Int. Ed*., **2014**, 53, 6905 |
| N-doped carbon | 0.83 (120 mV negative) | 0.68 (> 120 mV negative) | 3.3 | *J. Am. Chem. Soc*., **2014**, 136, 6790 |
| N, P-doped carbon fibres | 0.94 (50 mV negative) | 0.67 (130 mV negative) | not mentioned | *Angew. Chem. Int. Ed*., **2015**, 54, 4646 |

## References


[S1] P. Chen, L. Gu and X. B. Cao, CrystEngComm, 2010, 12, 3950; P. Chen, G. Li, X. Xue, Y. Song, L. Zhu and X. B. Cao, *Mater. Chem. Phys*., 2010, **122**, 41;

[S2] S. C. M. Piana and H. A. Gasteiger, *J. Electroanal. Chem.,* **2001**, *495*, 134; Y. Liang, Y. Li, H. Wang, J. Zhou, J. Wang, T. Regier and H. Dai, *Nat. Mater.,* **2011**, *10*, 780.

[S3] S. Wang, D. Yu, L. Dai, D. W. Chang and J. B. Baek, *ACS Nano,* **2011**, *5*, 6202.

[S4] W. Chaikittisilp, M. Hu, H. Wang, H. S. Huang, T. Fujita, K. C. Wu, L. C. Chen, Y. Yamauchi and K. Ariga, *Chem. Commun.* **2012**, *48*, 7259; H. X. Zhong, J. Wang, Y. W. Zhang, W. L. Xu, W. Xing, D. Xu, Y. F. Zhang and X. B. Zhang, *Angew. Chem., Int. Ed.* **2014**, *53*, 14235.

[S5] L. F. Lai, J. R. Potts, Da Zhan, L. Wang, C. K. Poh, C. H. Tang, H. Gong, Z. X. Shen, J. Y. Lin and R. S. Ruoff, *Energy Environ. Sci.* **2012**, *5*, 7936.

[S6] Z. Y. Sun, J. Masa, P. Weide, S. M. Fairclough, A. W. Robertson, P. Ebbinghaus, J. H. Warner, S. C. E. Tsang, M. Muhler and W. Schuhmann, *J. Mater. Chem. A* **2015**, *3*, 15444; W. Xia, C. Jin, S. Kundu and M. Muhler, *Carbon* **2009**, *47*, 919.

[S7] S. Yang, X. Feng, X. Wang and K. Müllen, *Angew. Chem. Int. Ed.* **2011**, *50*, 5339; J. Liang, Y. Jiao, M. Jaroniec, S. Z. Qiao, *Angew. Chem. Int. Ed.* **2012**, *51*, 11496.

[S8] T. N. Ye, L. B. Lv, X. H. Li, M. Xu and J. S. Chen, *Angew. Chem. Int. Ed.* **2014**, *53*, 6905.

[S9] D. H. Guo, R. Shibuya, C. Akiba, S. Saji, T. Kondo and J. Nakamura, *Science* **2016**, *351*, 361